

Analyzing Transient Turbulence in a Stenosed Carotid Artery by Proper Orthogonal Decomposition

LEOPOLD GRINBERG,¹ ALEXANDER YAKHOT,² and GEORGE EM KARNIADAKIS¹

¹Division of Applied Mathematics, Brown University, Providence, RI 02912, USA; and ²Department of Mechanical Engineering, The Pearlston Center for Aeronautical Engineering Studies, Ben-Gurion University, Beersheva 84105, Israel

(Received 8 December 2008; accepted 27 July 2009; published online 11 August 2009)

Abstract—High-resolution three-dimensional simulations (involving 100 million degrees of freedom) were employed to study transient turbulent flow in a carotid arterial bifurcation with a stenosed internal carotid artery (ICA). The geometrical model was reconstructed from MRI images, and *in vivo* velocity measurements were incorporated in the simulations to provide inlet and outlet boundary conditions. Due to the high degree of the ICA occlusion and the variable flow rate, a transitional and intermittent flow between laminar and turbulent states was established. Time- and space-window proper orthogonal decomposition (POD) was applied to quantify the different flow regimes in the occluded artery. A simplified version of the POD analysis that utilizes 2D slices only—more appropriate in the clinical setting—was also investigated.

Keywords—CFD, Transitional flow, Windowed-POD.

INTRODUCTION

We employ computational fluid dynamics (CFD) to investigate blood flow in a carotid artery, which has an occlusion in the cross-section area of its internal branch. The common carotid artery (CCA) transports blood from the arch of aorta (left CCA) or from the brachycephalic artery (right CCA) to the internal carotid artery (ICA) and external carotid artery (ECA); the latter carries blood primarily to the facial tissues while ICA supplies blood to the brain. Interruption in the blood flow to the brain may lead to a stroke. There are two major kinds of strokes¹⁵: (1) an ischemic stroke, caused by a blood clot that blocks or plugs a blood vessel or artery in the brain; and (2) a hemorrhagic stroke, caused by a bleeding vessel. According to the American Heart Association, the carotid disease is the major risk factor for ischemic stroke, caused by detachment of the plaque, which may clot vital brain

vessels. Atherosclerotic plaques inside an arterial wall result in a *local* occlusion of the artery lumen—a stenosis. The stenosis may trigger transition to turbulence, and onset of turbulence downstream of severe occlusions has been observed in laboratory experiments.⁸ It is now well established that transition to turbulence is expected to be dependent on flow pulsatility and on the geometry of the arterial wall. In particular, the effect of pulsatility on transition to turbulence is common in different arterial flows and many studies support this view.²⁰

Detection of arterial narrowing can be performed using catheter arteriography¹⁵; its pathophysiological relevance has been demonstrated empirically by the close correlation between the degree of stenosis and the subsequent risk of stroke. However, arteriography is an invasive procedure, and hence there is a need in developing non-invasive methods. Presently, diagnosis of an arterial occlusion is routinely performed by non-invasive techniques: computer tomography (CT), magnetic resonance (MR) or color Doppler ultrasound (CDUS) scanning. Audible sounds (carotid bruit), detected in the proximity of the carotid artery during auscultation may also indicate presence of stenosis.^{1,7} Weak correlation between the carotid bruit and stenosis was reported in Sauve *et al.*²⁶ but it was emphasized that the detection and diagnosis of the degree of occlusion cannot rely on auscultation only. In particular, high-frequency components of pressure oscillations may be attributed to wall movement and/or to turbulence. In our studies, we considered a *rigid* arterial wall model and hence the high-frequency oscillations predicted by our high-accuracy CFD simulations are of hydrodynamic origin, i.e., due to the turbulence *solely*, which is triggered by the stenosis.

Flow in a stenosed carotid artery has been studied experimentally^{2,4,19} and numerically.^{9,30,31} Here, we apply the proper orthogonal decomposition (POD) to analyze pulsatile transitional *laminar-turbulent* flows in a carotid arterial bifurcation. POD was introduced in

Address correspondence to George Em Karniadakis, Division of Applied Mathematics, Brown University, Providence, RI 02912, USA. Electronic mail: lgrinb@dam.brown.edu, George_Karniadakis@brown.edu

fluid mechanics in Lumley²³ for analyzing complex flow regimes, and a comprehensive review on application of the POD method in turbulent flow analysis can be found in Berkooz *et al.*⁵ Our focus is on the onset of turbulence and subsequent re-laminarization. Using high-accuracy CFD results, we demonstrate the capability of an extension of POD to identify the transitional and intermittent regimes in a stenosed carotid artery. We show that the behavior of the POD eigenvalue spectrum is directly related to the presence of turbulence and hence it can be used for its detection during the cardiac cycle. We also propose a method on how to extend the POD analysis to clinical measurements, e.g., by CDUS.

The paper is organized as follows. In section “[Methods](#)” we discuss the computational methods employed in this study. In section “[Results](#)” we discuss the patterns of transitional flow in the stenosed carotid artery, and present the *time-* and *space-window* POD for detecting turbulence. We also discuss the applicability of the window-POD in the clinical setting by comparing our high-resolution results with those mimicking medical images obtained with moderate resolution. In section “[Discussion and summary](#)” we conclude with a discussion and a brief outlook on the application of our method in the analysis of clinically measured data. In the [Appendix](#) we provide details on the resolution studies, the arterial geometry reconstruction, and the inlet/outlet boundary conditions.

METHODS

Modeling Transitional Flow in the Carotid Artery

Numerical simulations of blood flows in complex geometries are carried out mostly by employing the Reynolds-averaged Navier–Stokes (RANS) approach. Stroud *et al.*³¹ employed a low-Reynolds number two-equation turbulence model for a realistic carotid bifurcation but using its two-dimensional projection. In the three-dimensional geometry of arteries, the presence of high-degree stenosis and flow pulsatility greatly increase the probability that turbulence may be sustained even at relatively low Reynolds numbers.²⁰ Since the standard RANS models are derived for fully developed high Reynolds number turbulence, they are not appropriate for modeling transitional flow. Low Reynolds number RANS approaches have been validated using mostly simple geometry benchmarks and cannot give reliable results for cardiovascular flows. In general, RANS models cannot predict complex features of such flows because they may (a) erroneously generate turbulence, and (b) underestimate back-flow regions due to artificially increased dissipation by

overestimating the turbulent viscosity. A need, therefore, exists to extend computational studies of transitional flows through stenosed arteries by direct numerical simulation (DNS, simulation without applying *ad hoc* models) in three-dimensional (3D) realistic geometries. The first DNS results of a patient-specific carotid bifurcation were reported in Lee *et al.*²² and Grinberg *et al.*¹²

To perform three-dimensional DNS of flow through carotid artery we employed the high-order spectral/*hp* element code NEKTAR.¹⁷ Spectral/*hp* element spatial discretization provides high accuracy and is suitable for complex geometries; it is particularly effective in capturing intermittent laminar-turbulent regimes since it does not suffer from artificial dissipation. Other details can be found in the [Appendix](#). In the following, we present the computational setup.

Geometry, Computational Domain and Grid Generation

A geometric model of the carotid artery was obtained from *in vivo* MRI images shown in Fig. 1a processed by an in-house software package to generate a model of the arterial wall. Editing of the arterial geometry and subsequent mesh generation was performed using Gridgen—a commercial mesh generator developed by Pointwise.³⁵ In Fig. 1b we show the geometric model reconstructed from MRI images. In the current study we use a mesh with 22,441 tetrahedral spectral elements of variable size, and eighth-order polynomial approximation ($P = 8$) within each element, corresponding to 24,685,100 degrees of freedom (DOF) per variable. For consistent integration and for preventing aliasing—an important issue in resolving accurately the onset of turbulence—the 3/2-rule was applied in the calculation of the nonlinear terms in the Navier–Stokes equations.¹⁸ Thus, the total number of quadrature points in the computational domain was above 37 millions. A systematic resolution study was performed using *h*- and *p*-refinement techniques. Specifically, the spectral/*hp* element method provides a dual path to convergence (i.e., decay of numerical error) as follows: (a) *h*-convergence, with the accuracy of the solution depending on the size of elements; and (b) *p*-convergence with the accuracy depending on the order of the polynomial approximation. To enhance the accuracy, a local mesh refinement (*h*-refinement) was applied downstream of the ICA narrowing. Also, the flat faces of the surface elements were projected on smooth curved boundaries. In Fig. 1c we plot the parametric surface mesh (2D structured grid) at the carotid bifurcation and in Fig. 1d we show the computational grid projected on the curved surface. For temporal discretization, a second-order semi-implicit time splitting scheme was implemented.¹⁶

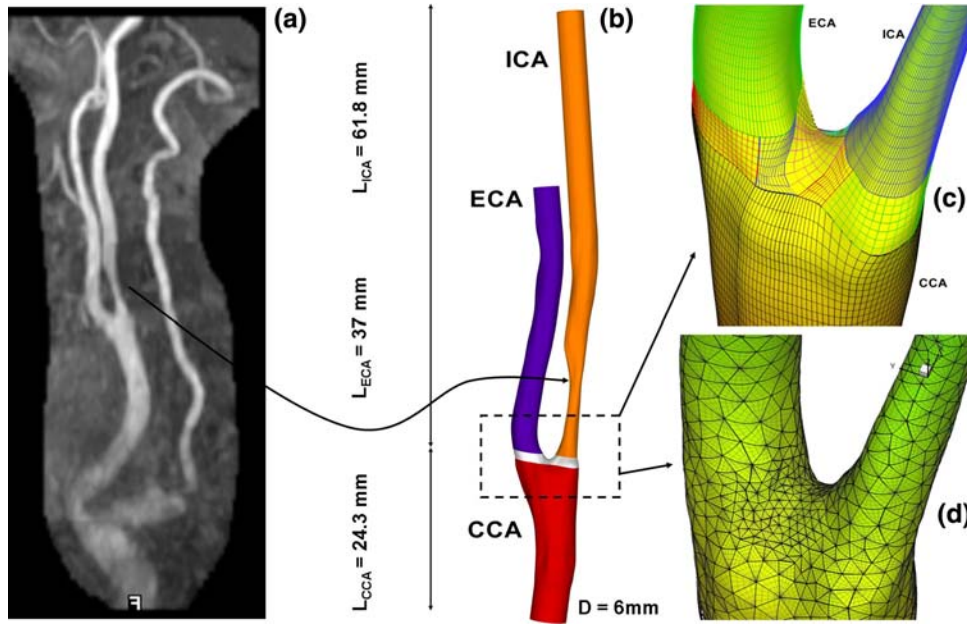


FIGURE 1. (in color) Reconstruction of arterial geometry from MRI images: (a) MRI of carotid artery (courtesy of Prof. M. Gomori, Hadassah, Jerusalem). (b) Geometrical model of a carotid artery; colors represent different arterial segments. (c) Patches of parametric surface representation, colors represent different patches. (d) Computational mesh, consistent with third-order polynomial approximation.

Proper Orthogonal Decomposition (POD)

POD is a very effective method for identifying an energetically dominant set of eigenmodes in an evolving system. It was originally introduced in fluid dynamics for identification of coherent structures in a turbulent velocity field. Sirovich²⁹ introduced the *snapshot* method to analyze large data sets. Application of POD for analyzing transient turbulence in cardiovascular flows was first reported by Grinberg *et al.*¹³

For a set of data $\mathbf{u}(\mathbf{x}, t)$, represented as a function of physical space \mathbf{x} and time t , POD determines a set of orthogonal basis functions of space $\phi_i^k(\mathbf{x})$ and temporal modes $a_k(t)$; here $i = 1, 2, 3$ is the coordinate index and $k = 1, 2, \dots, M$ is the mode index. The basis is sought so that the approximation onto the first K functions: $\hat{u}_i(\mathbf{x}, t) = \sum_{k=1}^K a_k(t) \phi_i^k(\mathbf{x})$, $K \leq M$ has the largest mean square projection. We shall use the method of snapshots to compute the POD modes in a time interval T . Here the inner product between every pair of velocity fields (snapshots) $C(t, t') = T^{-1} \int_{\Omega} \mathbf{u}(\mathbf{x}, t) \mathbf{u}(\mathbf{x}, t') d\mathbf{x}$ is the temporal auto-correlation covariance matrix $C(t, t')$ used as the kernel. The temporal modes $a_k(t)$ are the eigenvectors of the $C(t, t')$ matrix and are calculated by solving an eigenvalue problem of the form: $\int_T C(t, t') a_m(t') dt' = \lambda_m a_m(t)$. Using orthogonality, the POD spatial modes $\phi_i^k(\mathbf{x})$ are calculated by $\phi_i^k(\mathbf{x}) = T^{-1} (\lambda_m)^{-1} \int a_k(t) u_i(\mathbf{x}, t) dt$.

A spatio-temporal mode $a_k(t) \phi_i^k(\mathbf{x})$ represents a basic flow structure which has its own contribution to the total flow field. The eigenvalue of a single mode represents its contribution to the total kinetic energy of the flow field $\int_{\Omega} \langle u_i(\mathbf{x}) u_i(\mathbf{x}) \rangle d\mathbf{x}$, which is equal to the sum over all eigenvalues. Therefore, the eigenspectrum of the decomposition can be regarded as the primary information indicating the importance of each individual mode from the energetic point of view. The modes with the lowest numbers are the most energetic modes and correspond to coherent flow structures. Specifically, we define

$$E_M = \sum_{k=1}^M \lambda_k, \quad E_{n,m} = \sum_{k=n}^m \lambda_k, \quad (1)$$

where λ_k are the eigenvalues, E_M is the total kinetic energy and $E_{n,m}$ is the kinetic energy associated with the modes in the range n to mode m .

RESULTS

Problem Formulation and Computational Set-up

The computational domain consists of the common, internal and external carotid arteries (CCA, ICA and ECA, respectively). A fully developed velocity profile was prescribed at the proximal end of the CCA using superposition with the well-known Womersley

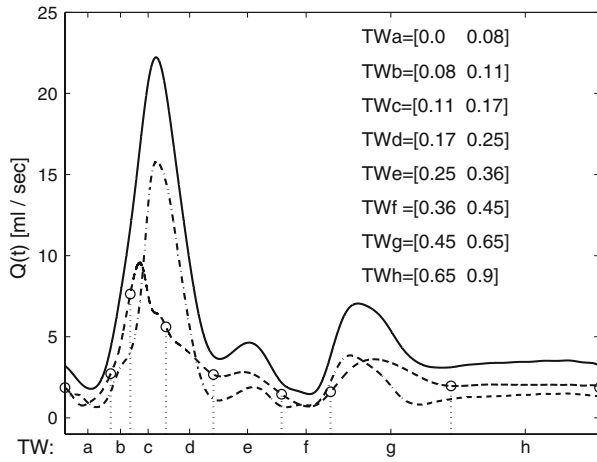


FIGURE 2. Waveform flow rates imposed in the CCA (solid), ICA (dash) and ECA (dash-dot) arteries and time-windows selected for POD data analysis.

analytical profile for each Fourier mode of the flow rate curve. To this end, the flow rate $Q(t)$ shown in Fig. 2 was approximated by $N = 20$ Fourier modes as $Q(t) = A_0 + \sum_{k=1}^N [A_k \sin(k\omega t) + B_k \cos(k\omega t)]$; here ω is the main frequency and A_0 , A_k , B_k are the coefficients of the Fourier expansion. At the distal end of the ICA and ECA, we used time-dependent *RC*-type boundary condition for the pressure,¹⁰ supplemented with the zero Neumann boundary condition for velocity. The degree of stenosis, S , in the ICA is defined as the ratio of the reduction in cross-sectional area due to stenosis, i.e., $S = 1 - (D_{\min}/D_{\text{ICA}})^2$, where D_{ICA} is the ICA effective diameter measured downstream of the stenosis, and the effective diameter D_{\min} is computed from the area at the stenosis throat: $A_{\min} = \pi D_{\min}^2/4$. The Reynolds ($Re = U_m D/\nu$) and Womersley ($Ws = 0.5D\sqrt{\omega/\nu}$) numbers are based on the parameters at the CCA inlet. Here, U_m is the average (in space and time) velocity, $\omega = 2\pi/T$ where T is the one cardiac cycle time interval, and ν is the kinematic viscosity. In our simulations: $S \approx 77\%$, $D = 6$ mm, $\nu = 3.283$ mm²/s and $T = 0.9$ s. Consequently, $Re = 350$ and $Ws = 4.375$. The time step was chosen to satisfy the CFL stability constraint and is very small due to the high spectral resolution, in the range of $\Delta t \in [5.2 \times 10^{-8}, 10^{-6}]$ s. This small time step allows accurate resolution of the high frequency flow oscillations. To ensure sufficient temporal resolution for the POD study, we save the velocity field with intervals of about 8.0×10^{-4} s. Starting with low-order spatial approximation and zero velocity initial field, we performed numerical simulations over one cardiac cycle. Then, the spatial and temporal resolutions were increased and the flow was simulated during two additional cardiac cycles; for analysis we used the results collected over the last cardiac cycle.

Flow Patterns

Back-flow

Atherosclerotic plaques usually occur in regions of branching and marked curvature, at areas of geometric irregularity, and also in regions where blood flow undergoes sudden changes in magnitude and direction resulting in back-flow regions. Specifically, back-flow regions occur in the vicinity of carotid bulb or stenosis. These regions are characterized by very low wall shear stress (WSS). The oscillating shear index (OSI), as defined by Ku *et al.*,²¹ is a dimensionless local measure that quantifies the time a particular wall region experiences back-flow during the cardiac cycle. More specifically, high values of OSI can reveal the location of the back-flow boundary where WSS is zero. Regions of both low WSS and high OSI are thought to be susceptible to intimal thickening and plaque formation that promotes atherogenesis at these important sites within the carotid arteries. In Fig. 3 (left), we show back-flow regions detected in the carotid bulb and the immediate proximal vicinity of stenosis; these back-flow regions are quite stable throughout the systole phase. Figure 3 (right) shows typical instantaneous pathlines; while in CCA and ECA pathlines are quite organized, those in ICA exhibit disorder in the post-stenotic region featuring a swirling pattern. In Fig. 3 we also show complex cross-stream secondary flows.

Jet Flow and Onset of Turbulence

Sherwin and Blackburn²⁷ performed 3D DNS to study instabilities and transition to turbulence in a straight tube with a smooth axisymmetric constriction, which is an idealized representation of a stenosed artery. They reported that steady flow undergoes a Coanda-type jet formation and turbulent transition exhibiting hysteretic behavior with respect to changes in Reynolds number. (The Coanda effect is understood as the tendency of a jet stream to adhere to a curved boundary wall.) The blood flow along the curved wall is accompanied with decrease of the pressure on the wall, dropping below the surrounding pressure and resulting in the attachment of the fluid flow to the wall. The wall jet consists of an inner region, which is similar to a boundary layer, and an outer region wherein the flow resembles a free shear layer. These layers interact strongly and form a complex flow pattern. The laminar Coanda jet has the tendency to follow the circumferential wall only for small angles. The rapid increase of pressure along the wall occurs due to the influence of the curvature of the wall and the adverse pressure gradient in the direction of flow leading to flow separation. In general, the wall jet flows are turbulent owing to the *low* critical Reynolds number.

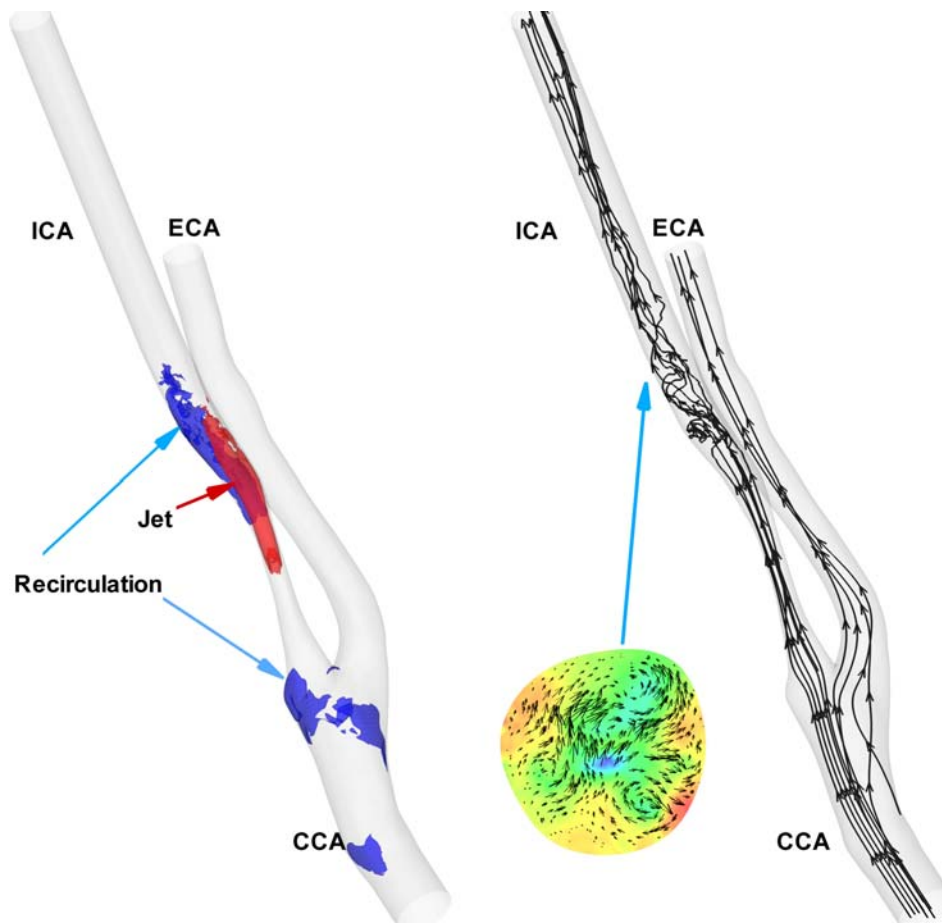


FIGURE 3. (in color) Flow patterns; left: iso-surfaces in a high-speed region (jet, red, $w = 4.2$ m/s), blue iso-surfaces—back-flow regions ($w = -0.04$ m/s); right: instantaneous path-lines of swirling flow and cross-stream secondary flows; color represents the pressure the maximum in-plane pressure difference is 3.62 mmHg.

Experimental and theoretical results have demonstrated that the instability of the entire wall jet is controlled by the outer region. Bajura and Catalano³ investigated experimentally transition to turbulence in planar wall jets, using flow visualization in a water tunnel. They observed the following stages in natural transition: (i) formation of discrete vortices in the outer shear layer; (ii) coalescence of adjacent vortices in the outer region, coupled with the rolling up of the inner shear layer; (iii) eruption of the wall jet off the surface of the flat plate into the ambient fluid (the “lift-off” stage); and (iv) dispersion of the organized flow pattern by three-dimensional turbulent motions.

Figures 4 and 5 demonstrate the jet-like effect created by the stenosis as predicted in our calculations. In Fig. 4 we show the contours of the Ω_y -vorticity (transverse) that can be linked to the rolling up along the wall (see coordinate axes in Fig. 4f), for different stages of transition that show the wall jet breakdown. These results illustrate the onset of turbulence due to shear layer type instabilities of the Coanda wall jet in

the post-stenotic region. Specifically, in Fig. 4a, the laminar state of the incoming flow is confirmed by the straight path traces. The jet outer region (marked by a blue trace) and the adjacent recirculation back-flow region (marked by a light-blue trace) form a free shear layer. In Fig. 4b, the jet moved downstream along the wall showing the early stage of interaction with the adjacent recirculation region. Figure 4c shows the perturbed shear layer at the leading edge of the jet. The tilted vorticity trace in Fig. 4d provides evidence of the stage of vortices coalescence in the outer region and the rolling up of the inner shear layer. The tilted wall jet rapidly breaks down leading to dispersion of the organized flow pattern (Figs. 4d and 4e). It should be noted that the breakdown gradually propagates upstream, a phenomenon that was predicted by Sherwin and Blackburn²⁷ using DNS in a simplified geometry. Figure 5 shows iso-surfaces of the longitudinal w -velocity (streamwise) component, depicting the stages when the coherent wall jet structure (Fig. 5a, green) collapses in the post-stenotic region (Fig. 5e).

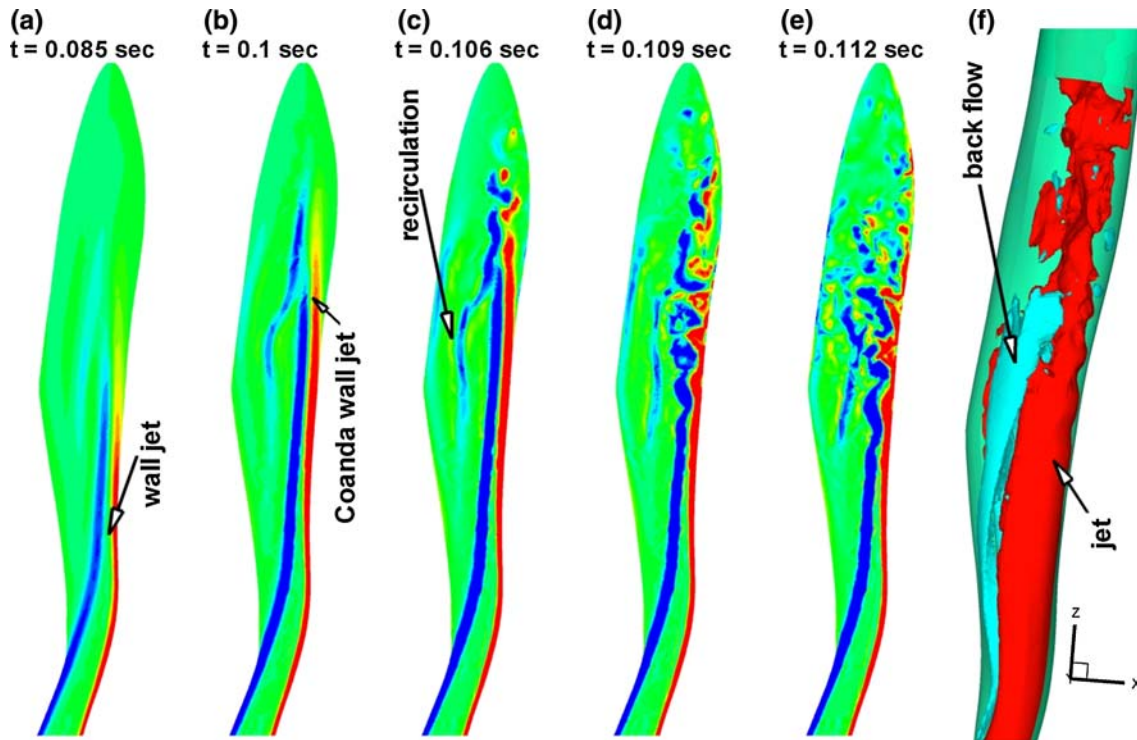


FIGURE 4. (in color) Unsteady flow in carotid artery: transition to turbulence. (a–e) Cross-flow non-dimensional vorticity contours Ω_y extracted along $y = -1.2$ in ICA. The colormaps corresponding to the vorticity data are: (a) blue $-1.7E+4 \text{ s}^{-1}$, red $+2.1E+4 \text{ s}^{-1}$; (b) blue $-3.4E+4 \text{ s}^{-1}$, red $+4.2E+4 \text{ s}^{-1}$; (c) blue $-4.2E+4 \text{ s}^{-1}$, red $+5.2E+4 \text{ s}^{-1}$; (d) blue $-4.7E+4 \text{ s}^{-1}$, red $+5.9E+4 \text{ s}^{-1}$; (e) blue $-5.1E+4 \text{ s}^{-1}$, red $+6.4E+4 \text{ s}^{-1}$; (f) region of ICA where flow becomes unstable, colors represent iso-surfaces of w -velocity (streamwise, along z -direction), $Re = 350$, $Ws = 4.375$.

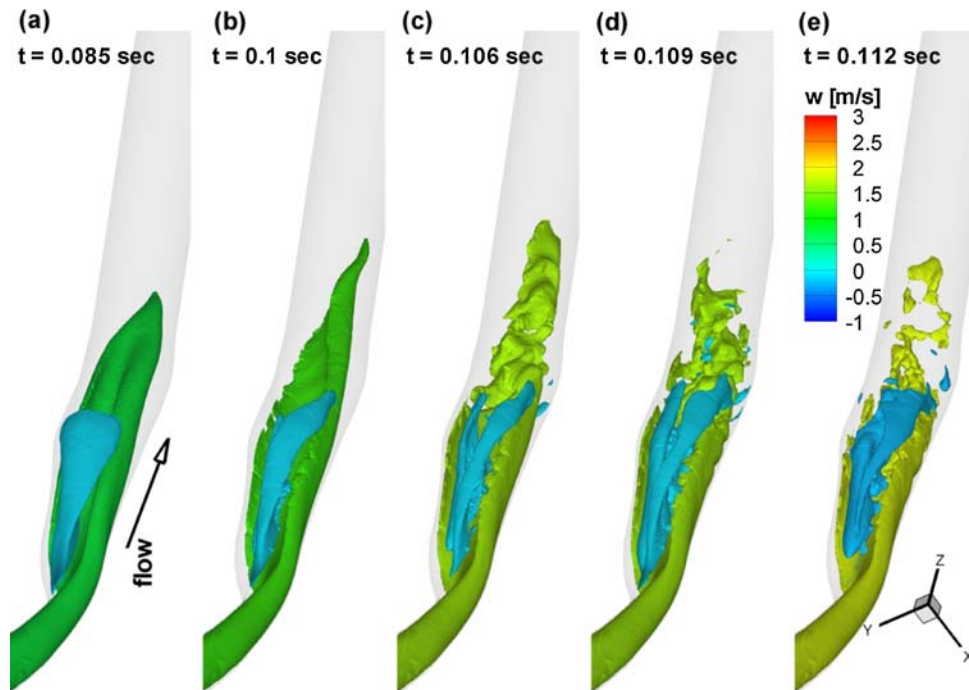


FIGURE 5. (in color) Wall jet formation and breakdown. Streamwise w -velocity iso-surfaces, blue indicates a back-flow recirculation region. $Re = 350$, $Ws = 4.375$.

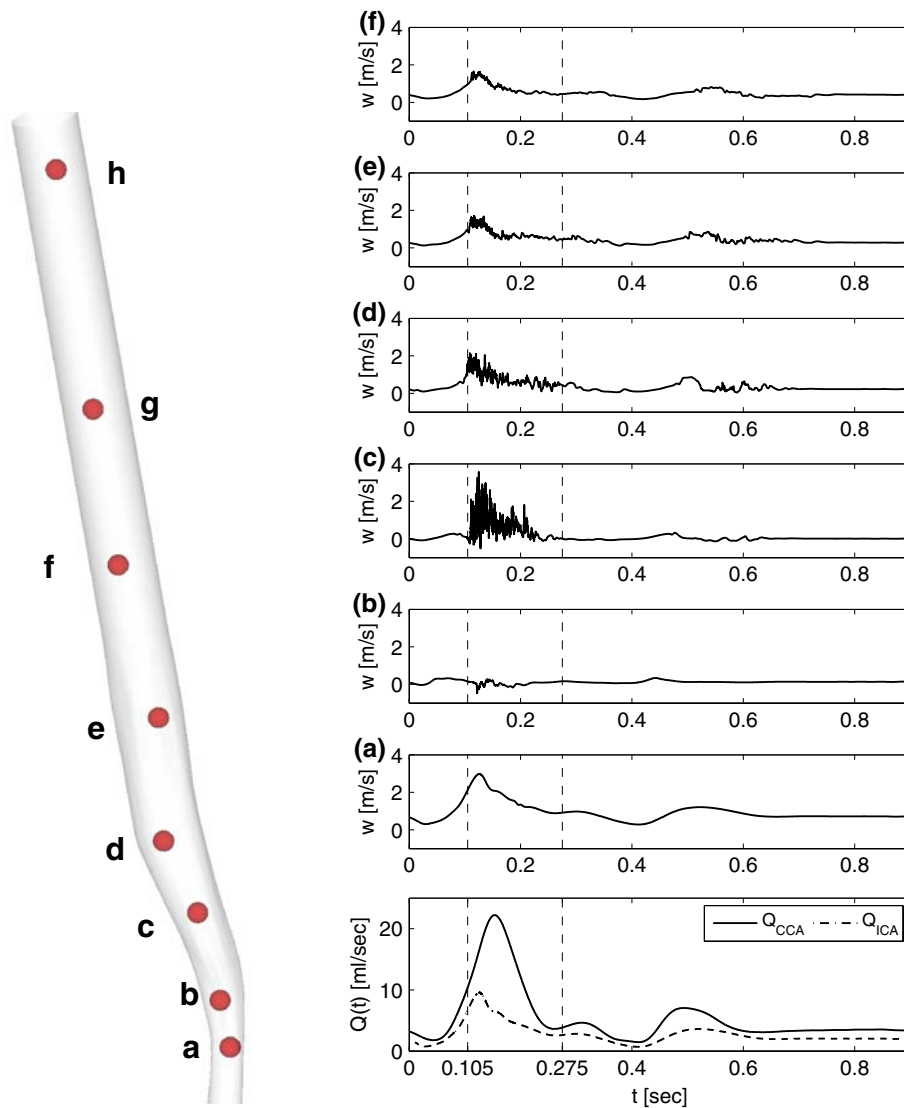


FIGURE 6. Time-traces of the streamwise w -velocity component at history points $a - f$ and flow rates at CCA and ICA; dash lines separate laminar and turbulent regimes, history points are marked by red dots.

We note that the recirculation region marked by the blue iso-surfaces, does not collapse, which implies that this region is quite stable.

Transient Turbulence Followed by Re-Laminarization

The transient turbulence regime changes the hemodynamic factors (e.g., wall shear stress, WSS). Specifically, it causes the WSS to vary significantly through the cardiac cycle; i.e., it becomes very high proximally to the stenosis throat in the ICA where the vulnerable plaque is usually built-up. For detection of turbulence in time and space, time traces of instantaneous axial velocity have been monitored along the ICA at several axial stations indicated in Fig. 6 (left). From Fig. 6c, the flow disturbances, as they appear during the

cardiac cycle, reveal that the turbulent state appears during the systolic phase and is localized in the post-stenotic region, with re-laminarization occurring farther downstream. To link the transition process to the time frame of the cardiac cycle, in Fig. 6 (right bottom plot) we also show the physiological flow rate waveforms in the CCA and ICA imposed in our calculations. The waveform curves consist of a brief systolic phase (acceleration and deceleration) and a longer diastolic phase with some increase in flow rate around $t \approx 0.55$. As follows from the time traces in Fig. 6c, the early turbulent activity in the post-stenotic region begins at the mid-acceleration phase of the cardiac cycle. In the early part of deceleration there is intense turbulent activity; past the mid-deceleration phase, the intensities die out and the flow begins to re-laminarize;

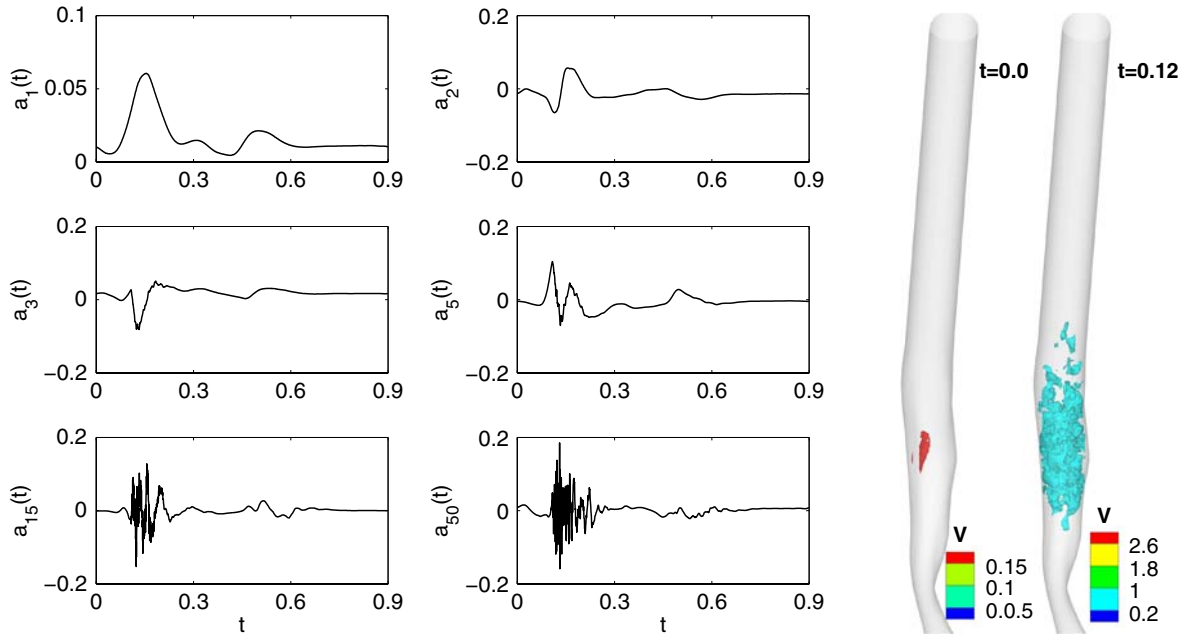


FIGURE 7. Left: temporal POD modes of velocity obtained over one cardiac cycle. Right: velocity field reconstructed from high-order POD modes $\tilde{u}_i(t, \mathbf{x}) = \sum_{k=3}^M [a_k(t) \phi_i^k(\mathbf{x})]$ at time instances $t = 0.0$ s and $t = 0.12$ s (systolic peak). Colors represent the corresponding iso-surfaces of $v = |\tilde{\mathbf{u}}|$. Only the ICA branch is shown. $M = 1125$, $Re = 350$, $Ws = 4.375$.

an exception is a short-term oscillation at $t \approx 0.55$. The transient turbulent regime lasts about 90% of a systole time, i.e., about 0.15 s or nearly 17% of the cardiac cycle.

POD Analysis

In this section we apply POD to detect turbulence in the stenosed carotid artery. The analysis is performed using two approaches: (a) POD based on the data collected over a *complete* cardiac cycle, and (b) *windowed* POD, that is the decomposition is performed over specific intervals of the cardiac cycle and also in different spatial 3D and 2D sub-domains. POD analysis performed over different time intervals shows clear correlation between transition to turbulence and the POD eigenspectrum. Analysis of the temporal and spatial modes of POD provides additional information regarding the onset of turbulence.

For statistically stationary turbulent flows, the time-averaged field can be calculated, and we can estimate how many POD modes are required to approximate the time-averaged field. The remaining modes can be attributed to the fluctuating turbulent field. In the POD analysis of the velocity field at high-Reynolds number obtained in Manhart,²⁴ the time-averaged flow field contained about 96% of the total kinetic energy which was primarily carried by mode $k = 1$. Thus, the remaining fluctuating modes ($k \geq 2$) were considered as “turbulent”. To extract the “turbulent” contribution

of the flow field in our simulations, we take advantage of the hierarchical feature of the POD decomposition. Specifically, in our calculations the energy associated with the first two POD modes, computed over a cardiac cycle, is about 96%, which we consider as the ensemble- (or phase) averaged field, and take the rest POD modes ($k \geq 3$) to represent the “turbulent” velocity field.

Detection of Turbulence by POD Analysis

As we already mentioned, the POD modes are hierarchical, with the first mode representing the main flow pattern and the higher modes adding finer features. In Fig. 7 (left) we plot selected temporal POD modes computed over one cardiac cycle at $Re = 350$. The first mode, $a_1(t)$, essentially follows the flowrate waveform imposed at the CCA inlet (Fig. 2). As in the time traces of the instantaneous axial velocity shown in Figs. 6b–6f, fluctuations of the higher modes indicate a transient turbulent regime throughout the systole phase. Short-duration weak oscillations around $t \approx 0.55$ that were recorded in time-traces in Fig. 6d are captured here by the high temporal modes. They are caused by a brief transition to turbulence due to a secondary acceleration-deceleration hump in the flow rate. In Fig. 7 (right), we show iso-surfaces of the velocity magnitude in the post-stenotic region reconstructed from the turbulent modes ($k = 3, 4, \dots, M$) at two different phases, peak-systole ($t = 0.12$) and

end-diastole ($t = 0.0$). The imprints of turbulence are clearly seen in the plot corresponding to $t = 0.12$, consistent with the turbulence activity detected by the high temporal modes.

Based on the aforementioned observations we draw the following conclusions: (i) The energy spectra of the velocity fields computed over the entire cycle do not reveal an intermittent laminar-turbulent regime. (ii) The transition to turbulence may be detected by analyzing the high-order temporal POD modes. (iii) The contribution of higher POD modes to the velocity field is not uniform in space, indicating *coexistence* of laminar and turbulent states.

Time- and Space-Window POD

The overall conclusion of the previous section is that POD analysis performed over a complete cardiac cycle and over the entire computational domain is inadequate to characterize space-intermittent turbulence in the transient flow regime. To this end, we suggest an alternative approach to analyze the intermittent and mixed flow regimes. Our goal is to measure the turbulent energy of flow in different *regions* of the domain and over different *time intervals*. In order to *quantify* the intensity of the turbulent flow we perform *windowed-POD* analysis in time and space. By analyzing the behavior of the temporal modes we may determine time intervals within which the flow is turbulent. Then, by performing POD analysis at different sub-domains, we can focus on regions where the energy associated with higher POD modes is significant. To characterize transitional flow we divide the cardiac cycle into eight *time-window* intervals denoted by *a* to *h* as illustrated in Fig. 2; the time-windows have been chosen to represent different stages of the transient regime. We will refer to the time-windows as TWa to TWh.

In Fig. 8 we plot the POD eigenspectra computed over six consecutive time-windows; the spectrum slope provides an indication of a turbulent or laminar regime. The spectra distinguish clearly the presence of transition from laminar to turbulent regime shown in Fig. 8a and followed by re-laminarization in Fig. 8b. The arrows in Fig. 8 denote the spectrum evolution in time: transition to turbulence is denoted by an upward-directed arrow, while the downward-directed arrow refers to re-laminarization. The spectra obtained over the TWc and TWD time-windows, covering the transitional regime, display a slow decay. The TWf and TWa time-windows belong to an end-diastole phase of the cardiac cycle; they are very similar and show a fast decay featuring a laminar regime. The results in Fig. 8 present a sequence of transient events in the post-stenotic flow, from laminar to turbulent, reverting

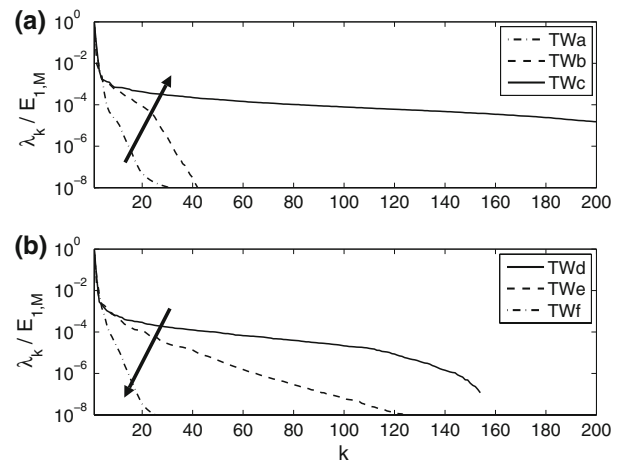


FIGURE 8. POD: eigenspectra obtained over different time-windows (see Fig. 2).

towards laminar, back again towards turbulent, and so on. To refine the POD analysis, in order to capture the transition to turbulence, we analyze individual temporal POD modes within a certain time-window. The first ten temporal modes corresponding to TWb are plotted in Fig. 9. The appearance of high frequency components at certain time intervals signifies the onset of turbulence.

Time-window POD analysis applied to transient flows reveals significantly more information than the full-cycle analysis. Moreover, unlike the complete cycle POD analysis, it is less expensive from the computational point of view. However, time-window POD is not sufficient to detect and characterize the spatially intermittent distribution of kinetic (turbulent) energy. As we have already observed, turbulent flow is not present over the entire domain of the stenosed carotid artery (see Fig. 7, right). Although visualization of certain POD modes helps to capture regions with high turbulent energy, it is not sufficient to *quantify* turbulence in each region, and alternative approaches should be applied. To this end, we employ *space-window* POD to detect regions with high kinetic energy. We analyze the eigenspectrum in three sub-domains of the ICA shown in Fig. 10: (1) the stenosis throat (sub-domain AB); (2) the post-stenotic region, from 12 to 22 mm downstream of the stenosis throat (sub domain CD); and (3) the post-stenotic region, from 32 to 42 mm downstream of the stenosis throat (sub-domain EF). Here we focus on the behavior of the first POD modes, hence the spectra in Fig. 10 are presented for the first 60 POD modes only.

The behavior of the POD eigenspectra in different sub-domains indeed reflects the characteristics of the flow: the rate of eigenspectra decay helps to distinguish between the regions with laminar and turbulent states. Specifically, in Figs. 10a and 10b we show fast decay of

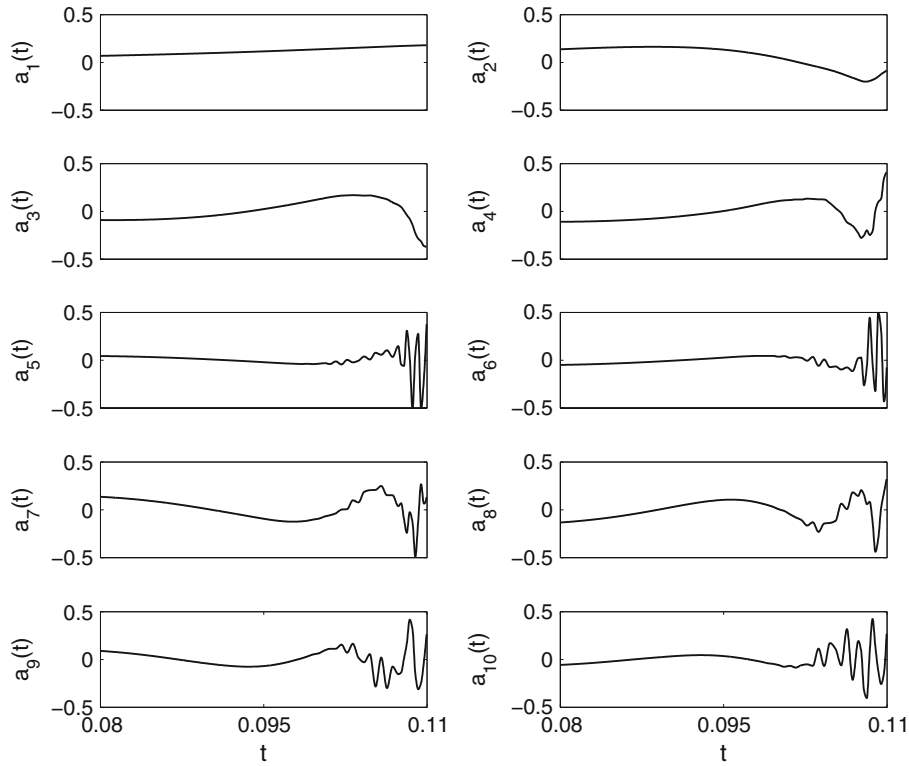


FIGURE 9. POD temporal modes $a_i(t)$, $i = 1, \dots, 10$ corresponding to the time window TWb (see Fig. 2).

the POD eigenspectra computed in sub-domain AB where no turbulence was detected. In Figs. 10c and 10d we plot the spectra computed in sub-domain CD . The energy spectra in Fig. 10c reveal onset of turbulence and subsequent flow re-laminarization. The spectra obtained over TWc and TWd depict slow decay, typical for turbulent flow. The POD spectra in Figs. 10e and 10f show the same scenario of transition/re-laminarization although the turbulence here is very weak because it decays and eventually re-laminarizes downstream of the stenosis (compare TWc and TWd curves in plots (e, f) with those in plots (c, d)).

POD in the Clinical Setting

Conventional clinical measurements provide two- and three-dimensional images. In this section we synthesize a collection of medical images by extracting them from CFD simulation data. Specifically, the velocity field computed in ICA is extracted from 2D slices (space-windows), and then time-window POD analysis is performed. First, we examine data sampled with high temporal resolution and, subsequently, we compare the results with those obtained with *reduced* sampling rates.

The velocity field computed in ICA is extracted along 2D slices (space-windows), and then time-window

POD analysis is performed. In Fig. 11 we show spectra computed over different time-windows using velocity fields obtained from a transverse to the main flow 2D slice at $z = 60$. Similarly to 3D POD analysis (see Figs. 10c and 10d), these POD spectra reveal transient flow regimes shown by arrows. POD spectra were also computed along longitudinal cross-sections mimicking an ultrasound image. In Fig. 12 we plot spectra obtained over different time-windows on a longitudinal slice located in the sub-domain CD . Comparison with the spectra obtained by high-resolution 3D POD analysis shows remarkable similarity (see Figs. 10c and 10d).

To quantify the *quasi-instantaneous* decay of the POD eigenvalues we propose the following procedure. We recall that turbulence is associated with existence of the high POD modes that exhibit a power law energy decay, namely

$$\lambda_k \sim k^{-s(t)}. \quad (2)$$

We extract flow field data from different planes, as shown in Figs. 11 and 12. For each time instant t over the cardiac cycle, POD analysis is performed over a relatively short time-window $t - \Delta t'/2 < t < t + \Delta t'/2$, where $\Delta t'$ was approximately 0.01 s at the systolic peak and approximately 0.1 s during the diastolic phase. Taking advantage of the high time resolution of our

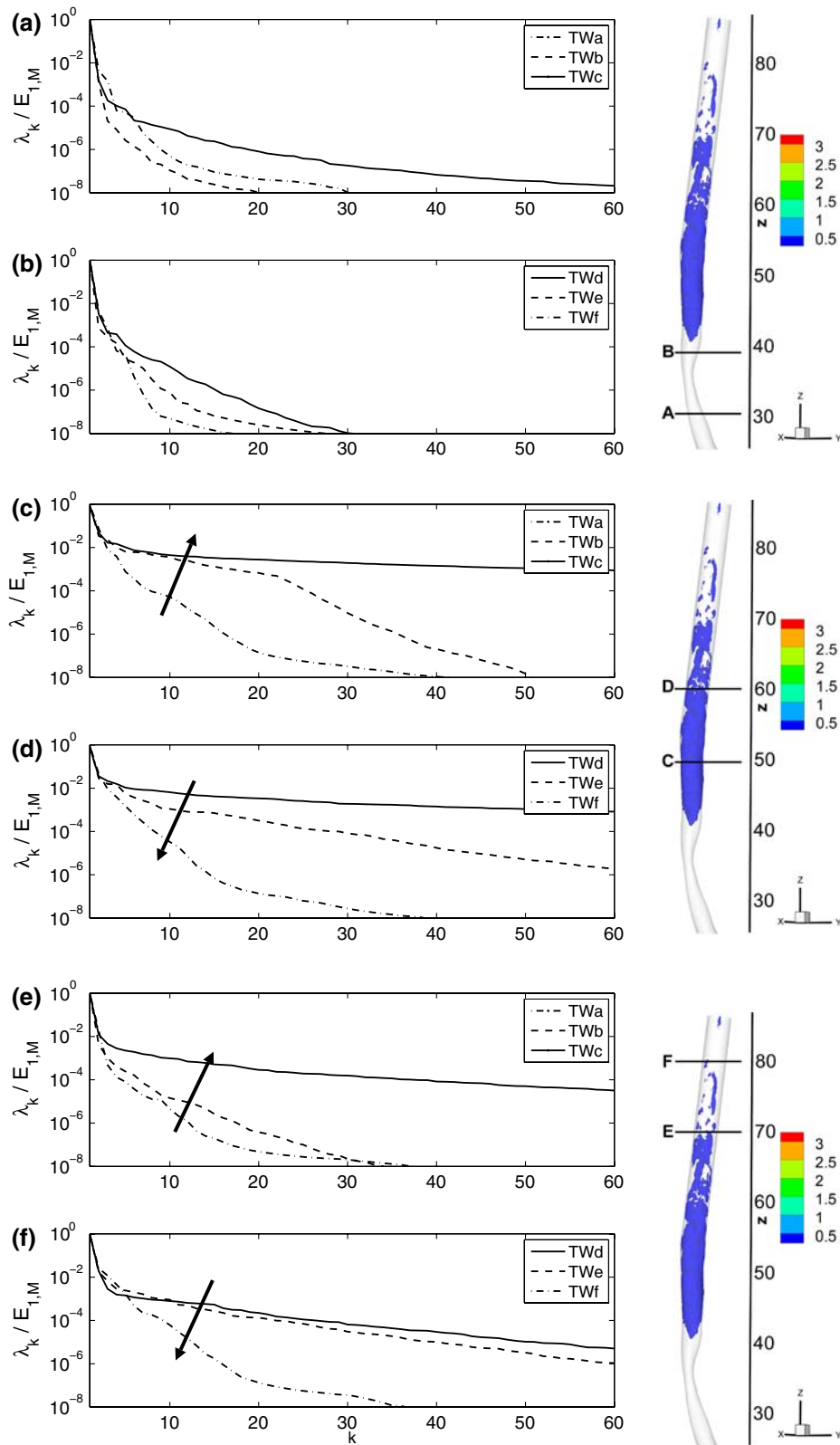


FIGURE 10. POD eigenspectra obtained over different time-windows in *sub-domains* AB, CD and EF (right): (a, c, e) time-windows TWa, TWb and TWc (flow acceleration and transition to turbulence); (b, d, f) time-windows TWd, TWe and TWf (flow deceleration and laminarization); (arrows show the time growth, color represents the w -iso-surface reconstructed from POD modes 20 to 50 at $t = 0.13$). The spectra are shown for the first 60 POD-modes only.

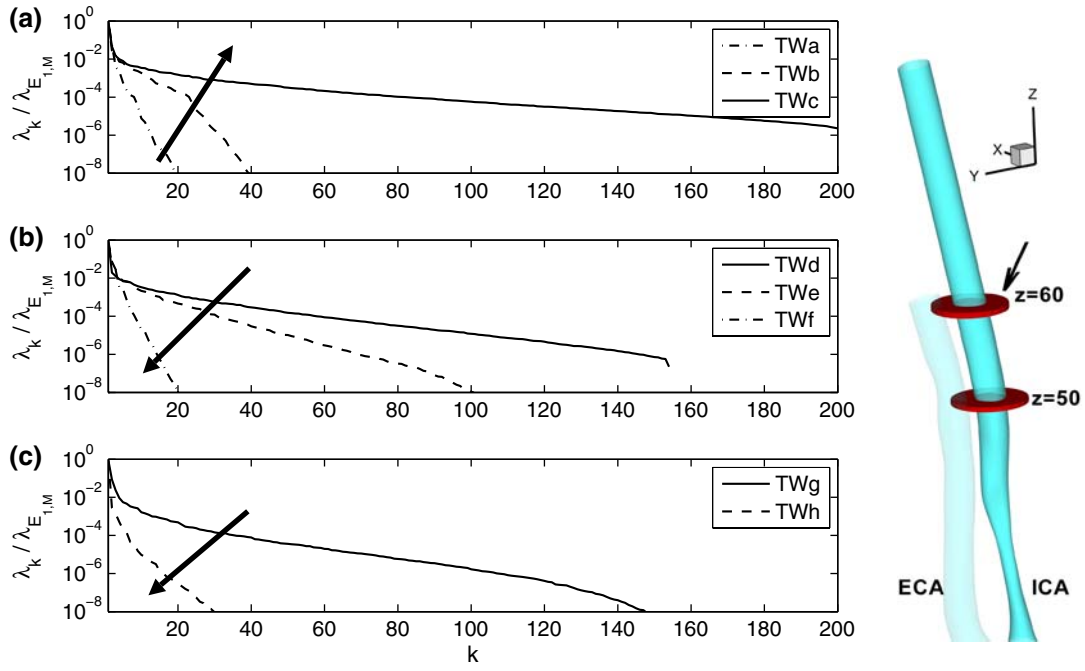


FIGURE 11. 2D POD: eigenspectra obtained over different time intervals (see Fig. 2); velocity field is extracted at $z = 60$; (a) time-windows TWa, TWb and TWc (flow acceleration, and transition to turbulence); (b) time-windows TWd, TWe and TWf (flow deceleration, and laminarization); (c) time-windows TWg and TWh (diastole phase); arrows show the time growth.

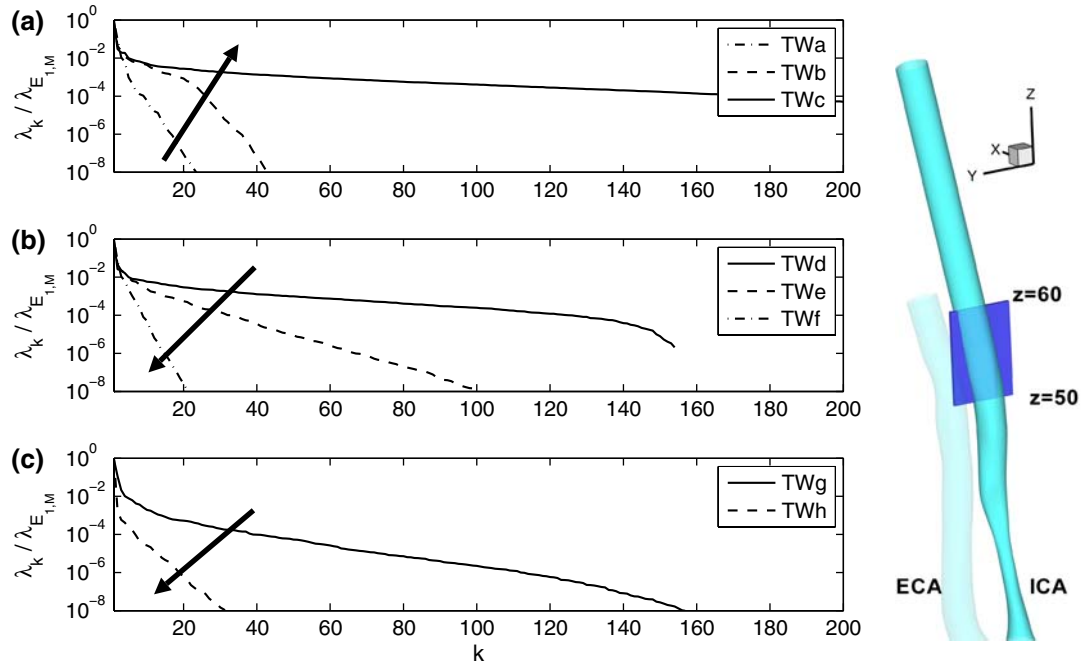


FIGURE 12. 2D POD: eigenspectra obtained over different time intervals (see Fig. 2). Velocity field is extracted on a slice with $x = \text{const}$, between $z = 50$ and $z = 60$; (a) time-windows TWa, TWb and TWc (flow acceleration, and transition to turbulence); (b) time-windows TWd, TWe and TWf (flow deceleration, and laminarization); (c) time-windows TWg and TWh (diastole phase); arrows show the time growth.

simulations, each time interval $\Delta t'$ was covered by 80 snapshots. The exponent $s(t)$ has been computed using first-order polynomial fitting and assuming

$\log_{10}(\lambda_k) = -s(t) \log_{10}(k)$, $k = 2, \dots, 10$. In Fig. 13 we plot the exponent $s(t)$ of the POD eigenvalues. The double hump curves clearly indicate the transient

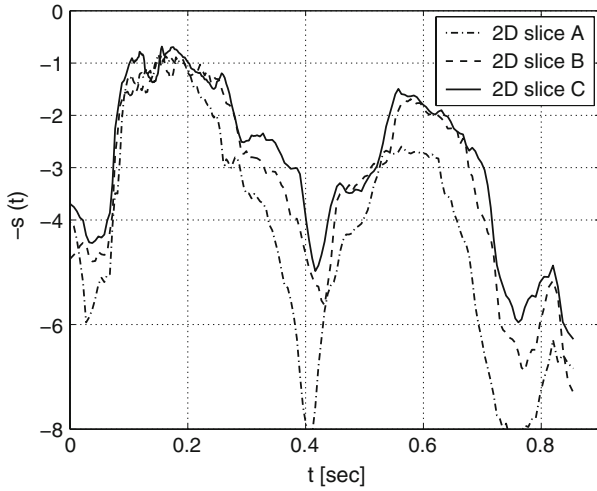


FIGURE 13. 2D POD: decay rate of POD eigenspectra. Data are extracted along: slice $z = 50$ (2D slice A) and slice $z = 60$ (2D slice B) depicted in Fig. 11 (right); slice with $x = \text{const}$ and located between $z = 50$ and $z = 60$ (2D slice C) shown in Fig. 12 (right). $s(t)$ is computed for the modes $k = 2 \div 10$.

nature of the flow. The low values of the slope ($0.8 < s < 1.1$) correspond to the turbulent regime that occurs during the systolic phase. The secondary turbulence regime at $t \approx 0.55$ mentioned above is also captured by the low slope values in Fig. 13.

Our CFD simulations were carried out with very high time resolution, allowing accurate estimation of the POD eigenspectrum. At the present time, there are serious limitations in the spatial and temporal resolution of MRI and CDUS imaging. MRI is a 3D technique for velocity imaging with high spatial resolution but low temporal resolution. CDUS images of a carotid artery are two-dimensional with time resolution of about 20–50 Hz. However, the sampling rate of the US devices is expected to grow significantly due to the introduction of parallel data processing. For example, owing to massive parallel beam formation, much higher frame rates can be achieved with a new cardiovascular platform SC2000 system launched recently by Siemens.²⁵ High temporal resolution of 481 Hz in US imaging (sample rate) is reported in Wang *et al.*³⁴ We note that several artifacts and noise contamination also occur during medical scanning, which may increase uncertainty in the data processing and lead to erroneous interpretations. As a first step, the artifacts and noise should be, if possible, identified and treated prior to using medical images for acquisition of clinical data.³⁶

To estimate if the suggested procedure can be used with relatively low time resolution imaging equipment we performed the following computations. We selected 800 time instants throughout the cycle and assumed

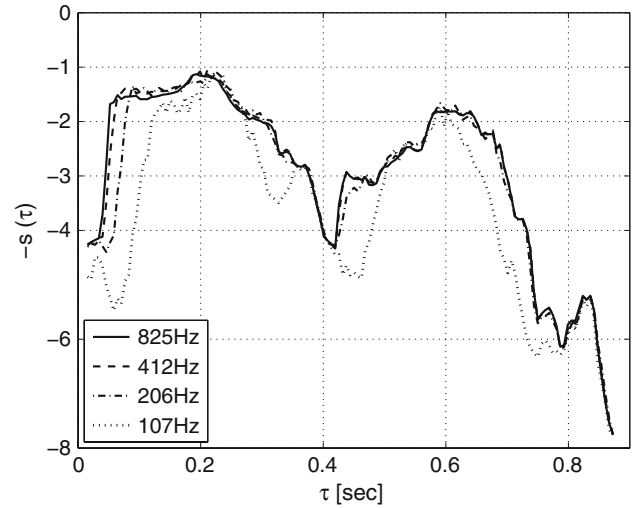


FIGURE 14. 2D POD: decay rate of POD eigenspectra, computed with variable temporal resolution. Data are extracted along the slice $z = 60$ (Fig. 11 right); $s(\tau)$ is computed for the modes $k = 2 \div 10$.

that each time instant τ corresponds to the middle of a time-window $\Delta\tau = [\tau_1, \tau_M]$, namely $\tau = (\tau_M + \tau_1)/2$. Here M is the number of snapshots within the time-window $\Delta\tau$ that depends on the imaging equipment time resolution. Specifically, we used $\Delta\tau \approx 0.12$ s, and, consequently, $M = 100$ and $M = 13$ corresponding to 825 and 107 Hz samplings, respectively. For each time-window, we computed the POD eigenspectra with different number of snapshots corresponding to different time resolutions. The decay rate $s(\tau)$ is shown in Fig. 14. We recall that the double hump shape of the $s(\tau)$ curve points to the transient turbulent regime. From Fig. 14, all spectra, even those obtained with 107 Hz, are representative of the transitional regime. A certain drawback of the low resolution data is that the $s(\tau)$ curve shows late transition and early re-laminarization. For example, the regime at $\tau = 0.11$ is turbulent, as we have seen in the previous sections, however, the corresponding time-window, $\Delta\tau = [0.05, 0.17]$, covers the laminar part of the cycle $0.05 < t < 0.09$. For the 107 Hz sampling, the number of snapshots within an interval $\Delta\tau$ is only 13 which means that the sampling includes only very few snapshots of the turbulent state. The same considerations explain the early re-laminarization at $\tau = 0.6$. On the other hand, the decay rate computed at $\tau = 0.11$ with 206 Hz data shows good agreement with that computed with 825 Hz data although it also predicts a slight delay of transition. Analyzing the $s(\tau)$ curves in Fig. 14 and taking into account the rapid growth of the medical imaging equipment time resolution, we can be optimistic that the windowed-POD technique can be applied to analyze

transient turbulence in stenosed vessels in the not-distant future.

DISCUSSION AND SUMMARY

In this paper we have performed high-resolution simulations to study transitional flow in a stenosed carotid artery alternating between laminar and turbulent states. The high degree of narrowing in the ICA (about 77%) creates a jet flow, which attaches to the wall of the artery and at certain (instantaneous) value of the Reynolds number becomes unstable leading to onset of turbulence. In particular, a mixed flow state is characterized by regions of unsteady laminar flow and a sub region of turbulence, starting downstream of the stenosis and extending about five to six centimeters farther downstream. As the Reynolds number decreases, flow re-laminarization in this sub-region takes place.

Studies of transitional flow in stenosed vessels with axi-symmetric and eccentric narrowing presented in Sherwin and Blackburn,²⁷ Cassanova and Giddens,⁶ Varghese *et al.*³² suggest that transition to turbulent flow appears at Reynolds number $Re > 500$ and Womersley number $Ws > 7.5$, i.e., at values higher than the ones in our simulations; however, this is due to the geometric complexity. For example, Varghese *et al.*³² observed that introducing slight eccentricity to the stenosis led to intermittent laminar-turbulent flow, which was not the case for flow in a pipe with an axi-symmetric constriction. This finding implies that due to arterial *geometric variability* among different patients with a stenosed ICA, transition to a turbulent state *may or may not* take place even if these patients have the same degree of stenosis or similar heart rate. Moreover, geometrical modifications, e.g., arterial deformations due to neck bending or twisting may trigger the onset of turbulence.

The specific focus of our work is *quantification* of transitional blood flow. The presence of fluctuations is not sufficient evidence for the presence of turbulence, which is characterized by specific statistical properties, and hence the distribution of energy between different scales is a commonly used criterion. To this end, we applied POD to cross-correlate flow fields at different times; laminar flows exhibit high degree of correlation while turbulent flows show lower correlation. The degree of correlation between velocity fields from different times can be measured by the rate of decay of the eigenvalues of the correlation matrix. The *value* of POD analysis of blood flow is in identification and characterization of arterial segments with high turbulent energy and hence of associated pathologies. If the region of turbulent flow is very small compared to the

size of the full domain considered, analysis of POD spectra or inspection of temporal modes performed on the entire domain is insufficient. To this end, we developed a time- and space-window POD version that can quantify precisely the kinetic energy associated with different POD modes. In CFD simulations this can be done with either 3D or 2D sub domains while in the clinical setting 2D images obtained via CDUS can be used. This approach can be compared to the window-FFT method or the wavelet decomposition, where a frequency spectrum is analyzed over a certain time interval.

POD analysis of high-Reynolds number turbulent flows was applied in Manhart²⁴ to flow around a wall-mounted hemisphere and by Yakhot and Liu (unpublished) to a wall-mounted cube. Both studies clearly showed the power law decay rate $s = -3/4$ of the POD high eigenvalues. The fact that the same power law was obtained in two different POD studies is intriguing, however, the precise value of the exponent is probably not universal. Fourier analysis applied to turbulent fields shows that the energy spectrum follows a power law $\lambda_k \sim k^{-s}$ with $1 < s < 3$ depending on the turbulence nature. For homogeneous isotropic turbulence, the POD eigenmodes are simply Fourier modes. The flow in the carotid is neither homogeneous nor isotropic but a power law energy decay provides additional evidence for the presence of turbulence. The time-space-window POD analysis of a flow in stenosed carotid artery presented in this paper reveals that during the systolic peak of the cardiac cycle the exponent s is in the range of $s = 1.1$ to $s = 0.8$ which is comparable to the results of Manhart²⁴ and Yakhot and Liu.

The window-POD procedure is computationally favorable and can be carried out very fast using a standard laptop. In contrast, the three-dimensional POD analysis of turbulent flow in a relatively large computational domain is computationally expensive. For example, in our study the data was computed at 24 million quadrature points. The computational work associated with POD (numerical integration) is not very high, however, the memory requirements are quite substantial. In our simulation the estimated memory requirement for POD analysis in the entire domain and over a one cardiac cycle was 400 GB. POD analysis of 1125 snapshots required about 60 minutes on the 128 AMD Opteron 2.6 MHz CPUs of the CRAY XT3 computer with 4 GB memory per processor; this time also includes the input of velocity and pressure fields and output of data for subsequent visualization. However, the *window-POD* analysis is computationally much more favorable and can be performed on a standard desktop computer in about 5 min.

The POD method for analysis of transitional flow in arteries has some limitations. The *accuracy* of POD analysis as clinical diagnostic tool depends on the spatio-temporal resolution of medical imaging devices, which at the present time may be sufficient to adequately capture laminar flows but it is not clear that it can capture mixed or fully turbulent regimes. In future work, we are planning to investigate this important issue using clinical data. Also, in the present work we have applied the utility of the time-space window POD method to analyze flow in *rigid* arteries. Although, arterial walls affected by atherosclerosis are less elastic than the healthy ones, POD should be extended to analyze flow in flexible vessels. Of interest would be how the transition scenario described in the present work is modified by the arterial wall movement.

APPENDIX

Solver

For solution of Navier–Stokes equations we use the parallel numerical solver NEKTAR which is based on the high-order spectral element/*hp* method.¹⁷ The computational domain consists of structured or unstructured grids or a combination of both. In each element the solution is approximated in terms of hierarchical mixed-order Jacobi polynomials. NEKTAR employs up to a third-order splitting scheme,¹⁶ that decouples the velocity and pressure fields. The solution of three Helmholtz equations for the velocity components and Poisson equation for the pressure are obtained iteratively using a Preconditioned Conjugate Gradient solver; in this study a new parallel low energy basis preconditioner^{11,28} was implemented which has the parallel efficiency of a diagonal preconditioner but it is almost a ten-fold faster.

Geometry Reconstruction

A geometric model of the carotid artery was obtained from *in vivo* MRI images shown in Fig. 1a. In particular, MRI images of cross-sectional slices of the left common carotid (CCA), internal carotid (ICA) and external carotid (ECA) arteries were acquired by a Genesis Signa scanner using a 3D time-of-flight (TOF) sequence. The distance between the slices was 1.2 mm and a total of 145 images was acquired.

In order to obtain the required contours, the cross-sectional views of MRI images were processed by an in-house software package, a Matlab-based GUI which allows *accurate* detection of the arterial wall. The end product is a geometric model of the arterial

wall saved in PLOT3D or STL format and is compatible with different mesh generation softwares. We use Gridgen—a commercial mesh generator developed by Pointwise,³⁵ which also allows editing and construction of geometric databases. In Fig. 1a the medical image of stenosed carotid artery is presented while in Fig. 1b we show the geometric model reconstructed from MRI images.

In the current study, a mesh with 22,441 tetrahedral elements was created; in the reference element a Cartesian grid based on Gauss quadrature points is generated. We employ Gauss–Lobatto quadrature points in one direction and Gauss–Radau points in the other two directions and compute the number of degrees of freedom (DOF) in each element as a number of quadrature points required for exact integration of quadratic terms. For eighth-order polynomial expansion we have $\text{DOF} = (P + 3) * (P + 2)^2 = 1100$ per element, that is a total number of DOF per *one* variable in our simulation is 24,685,100. In addition, we employed the 3/2 over-integration rule for consistent integration and more accurate differentiation of the nonlinear term,¹⁸ thus the number of quadrature points in the domain was above 37M. Local mesh refinement was applied downstream of the ICA narrowing. The flat faces of the surface elements were projected on smooth curved boundaries. The information on the wall curvature was provided by patches of parametric surfaces and also by a surface smoothing technique described in Volino and Magnenat-Thalmann.³³ In Fig. 1c we plot the parametric surface mesh (2D structured grid) at the carotid bifurcation and in Fig. 1d we provide an illustration of the computational grid, where the number of quadrature points inside each element is shown for a third-order polynomial approximation.

Resolution Study

Systematic resolution studies were performed. We used the *h*- and the *p*-type of refinement to minimize the error due to the spatial-discretization. The computational grid was refined in the regions with high velocity gradients; specifically, about 25% of the elements are located in a small fraction of ICA downstream the stenosis. The accuracy was verified by *p*-refinement. First, we performed unsteady 3D flow simulation in a pipe with $Re = 350$ and $Ws = 4.375$; a Womersley velocity profile was prescribed at the inlet, and zero pressure boundary condition at the outlet. Spectral convergence in Wall Shear Stress (WSS), presented in Fig. 15 (left), was obtained. Second, we performed steady flow simulation in the domain of carotid artery with parabolic flow profile at the inlet and zero pressure boundary conditions at both outlets.

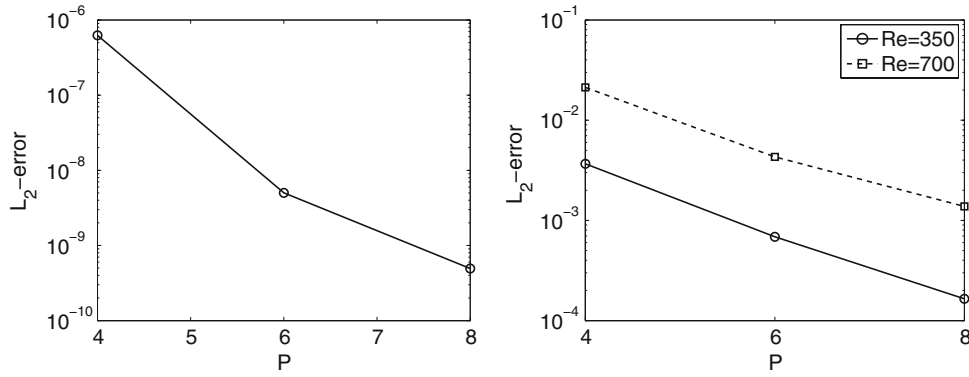


FIGURE 15. Verification of accuracy: convergence in the WSS. The magnitude of the (non-dimensional) WSS is of order $O(1)$. Simulations performed with $P = 4, 6, 8, 10$, $\Delta t = 0.0002$. Solution with $P = 10$ is considered as a reference solution. Left: unsteady flow in pipe, $Re = 350$, $Ws = 4.375$. Right: steady flow in carotid artery, $Re = 350$ and $Re = 700$.

TABLE 1. Verification of accuracy: steady flow simulations with $Re = 350$ and $Re = 700$.

P	$Re = 350$			$Re = 700$		
	u	v	w	u	v	w
4	9.72e-5	9.4e-5	2.17e-4	7.44e-4	7.11e-4	1.56e-3
6	1.38e-5	1.29e-5	2.58e-5	1.47e-4	1.39e-4	3.08e-4
8	3.14e-6	3.19e-6	6.68e-6	3.85e-5	3.60e-5	7.68e-5

Convergence of velocity field. L_2 -error normalized by the volume of computational domain. Solution performed with $P = 4, 6, 8, 10$, $\Delta t = 0.0002$. The solution with $P = 10$ is considered as a reference solution. The magnitude of the non-dimensional velocity components is of order $O(1)$.

The L_2 -error in velocity field is presented in Table 1. The L_2 -error in the WSS, depicted in Fig. 15 (right), shows spectral convergence. In both cases the WSS computed with the highest resolution was treated as a reference solution. We note that the discretization error in WSS is at least one order higher than the error in the velocity field. In general, it is a very difficult task to obtain spectral convergence in the WSS in a domain with complex geometry and curved boundaries, e.g., the domain of carotid artery.

Boundary Conditions

The following boundary conditions were applied: At the inlet the Womersley velocity profile was imposed, consistent with the wave form of the flowrate range reported in Holdsworth.¹⁴ The main characteristic parameters are: mean Reynolds number at inlet $Re_m = 350$, the minimum and maximum of the Reynolds number at inlet are $Re_{\min} = 46$ and $Re_{\max} = 1345$; and the Womersley number $Ws = 4.375$.

At the outlets we used time-dependent RC-type boundary condition for the pressure supplemented

with the zero Neumann boundary condition for velocity.¹⁰ This type of boundary condition provides an accurate and numerically efficient method to specify the flow rate ratio in numerical simulations of unsteady flow in a domain with multiple outlets. The pressure at outlet j is computed from

$$P_j(t) = -R_j(t)C_j \frac{dP_j}{dt} + R_j(t)Q_j(t), \quad (3)$$

where $R_j(t)$, C_j and $Q_j(t)$ are the specified resistance, capacitance and computed flow rate at the outlet j at time t . In a domain with two outlets, the required ratio $Q_1(t)/Q_2(t)$ is achieved by fixing one of the resistance values, for example $R_1 = \text{const}$, and computing the resistance at the second outlet from $R_2(t) = R_1 f(t)$ where $f(t) = Q_1(t)/Q_2(t)$. In this study we used $R_1 = R_{ICA} = 100$, $C_1 = 0.002$, $C_2 = 0.005$; the capacitance C_j is selected to effectively filter the high frequency flow rate oscillations at outlets which are due to numerical discretization and turbulence. The function $f(t)$ was computed as a scaled ratio of velocity, measured with Doppler Ultrasound in ECA and ICA. The clinical data is presented in Fig. 16. The measurements of velocity in ICA and ECA were not synchronized, which results in the obvious difficulty on how to impose the correct phase shift between the two wave forms. In order to compensate for the missing parameters two simulations were performed. In the first simulation the systolic peak in ICA precedes the one in ECA whereas in the second simulation it lags. The waveforms of inlet and outlet flow rates for the two cases are presented in Fig. 17. The major difference between the two sets of waveforms is the phase shift between the flow rates at the two outlets; consequently the onset of turbulence and re-laminarization occurred at slightly different times with respect to the beginning of the cardiac cycle. In both simulations we observed transitional flow; window-POD analysis

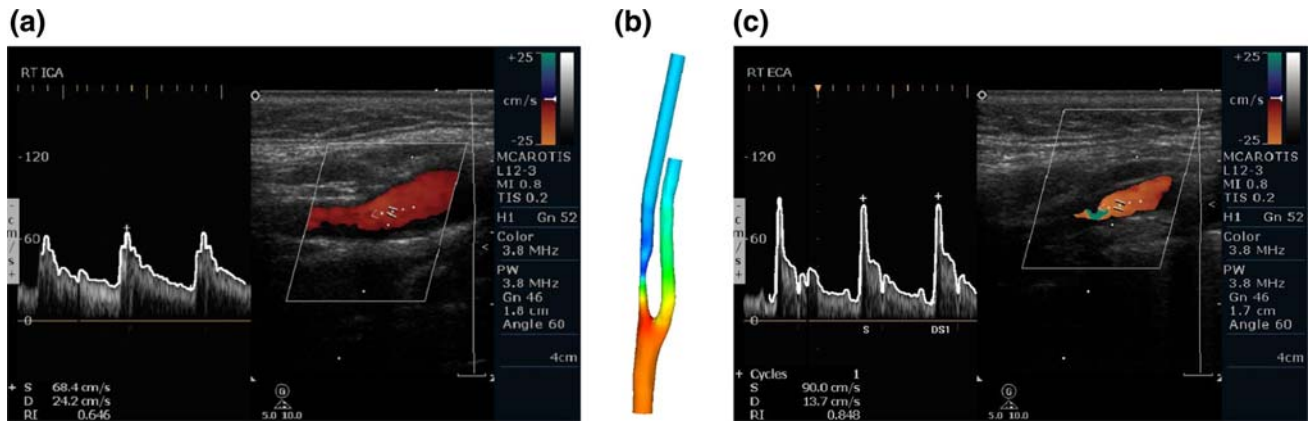


FIGURE 16. (in color) Doppler ultrasound measurements: Velocity wave in internal (left) and external (right) carotid arteries. Left side of plots (a) and (c) shows the monitored velocity; the wide white line highlights its maximum. In the middle of each frame the 2D image of instantaneous flow in arterial segment is captured; it depicts the relative (to the flow) direction of the ultrasound signal, the two short lines positioned inside the vessel point to the spatial location where the velocity was monitored. (b) Geometry of the carotid artery; colors represent pressure.

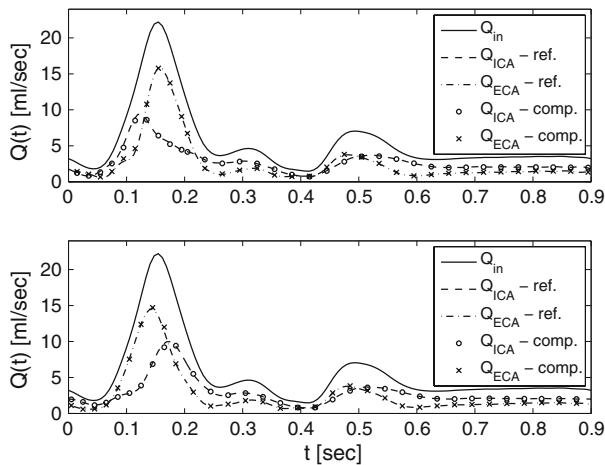


FIGURE 17. Simulation of intermittent laminar-turbulent-laminar flow in stenosed carotid artery with $R(t)$ C-type boundary condition: flow rates in CCA, ICA and ECA. The upper plot shows the case where the peak velocity at ICA precedes the one in ECA; the lower plot shows the alternative scenario. Prescribed (reference) values of the flow rates are marked with lines; computed values of the flow rates are marked with circles. $R_{ICA} = 100$, $R_{ECA}(t) = R_{ICA}(Q_{ICA}(t)/Q_{ECA}(t))$, $C_{ICA} = 0.002$, $C_{ECA} = 0.005$, $\text{mean}(Re_{inlet}) = 350$, $\text{min}(Re_{inlet}) = 46$, $\text{max}(Re_{inlet}) = 1345$, $Ws = 4.375$.

applied to two data sets produced similar results, hence in this paper we present results of the first simulation only.

ACKNOWLEDGMENTS

This work was supported by the National Science Foundation under grants OCI-0636336 and OCI-0845449. Supercomputer resources were provided by

the NSF Large Resource Allocations Committee at Pittsburgh Supercomputing Center and Texas Advanced Computing Center.

REFERENCES

- 1Akay, Y. M., M. Akay, W. Welkowitz, S. Lewkowicz, and Y. Palti. Dynamics of the sounds caused by partially occluded femoral arteries in dogs. *Ann. Biomed. Eng.* 22:493–500, 1994.
- 2August, A. D., B. Ariff, S. A. G. McG. Thom, X. Y. Xu, and A. D. Hughes. Analysis of complex flow and relationship between blood pressure, wall shear stress, and intima-media thickness in the human carotid artery. *Am. J. Physiol. Heart Circ. Physiol.* 293:1031–1037, 2007.
- 3Bajura, R. A., and M. R. Catalano. Transition in a two-dimensional plane wall jet. *J. Fluid Mech.* 70:773–799, 1975.
- 4Bale-Glickman, J., K. Selby, D. Saloner, and O. Savas. Experimental flow studies in exact-replica phantoms of atherosclerotic carotid bifurcations under steady input conditions. *J. Biomech. Eng.* 125(1):38–48, 2003.
- 5Berkooz, G., P. Holmes, and J. L. Lumley. The proper orthogonal decomposition in the analysis of turbulent flows. *Ann. Rev. Fluid Mech.* 25:539–575, 1993.
- 6Cassanova, R. A., and D. P. Giddens. Disorder distal to modified stenoses in steady and pulsatile flow. *J. Biomech.* 11:441–453, 1978.
- 7Chungcharoen, D. Genesis of Korotkoff sounds, *Am. J. Physiol.* 207:190–194, 1964.
- 8Clark, C. The propagation of turbulence produced by a stenosis. *J. Biomech.* 13:591–604, 1980.
- 9Fischer, P. F., F. Loth, S. E. Lee, S. W. Lee, D. Smith, and H. Bassiouny. Simulation of high Reynolds number vascular flows. *Comput. Methods Appl. Mech. Eng.* 196:3049–3060, 2007.
- 10Grinberg, L., and G. E. Karniadakis. Outflow boundary conditions for arterial networks with multiple outlets. *Ann. Biomed. Eng.* 36(9):1496–1514, 2008.

- ¹¹Grinberg, L., D. Pekurovsky, S. J. Sherwin, and G. E. Karniadakis. Parallel performance of a low energy basis preconditioner for spectral/hp elements. *Parallel Comput.* 35(5):284–304, 2009.
- ¹²Grinberg, L., A. Yakhot, and G. E. Karniadakis. DNS of flow in stenosed carotid artery. 59th Annual Meeting of the APS, Division of Fluid Dynamics, Tampa, FL, 2006.
- ¹³Grinberg, L., A. Yakhot, and G. E. Karniadakis. Onset of turbulence in stenosed carotid artery. International Conference of the Engineering Mechanics Institute (EM08), Minneapolis, MN, 2008.
- ¹⁴Holdsworth, D. W., C. J. D. Norley, R. Frayne, D. A. Steinman, and B. K. Rutt. Characterization of common carotid artery blood-flow waveforms in normal human subjects. *Physiol. Meas.* 20:219–240, 1999.
- ¹⁵http://www.ninds.nih.gov/find_people/groups/stroke_prg/04_2002_stroke_prg_report.htm. Accessed 2 August 2009.
- ¹⁶Karniadakis, G. E., M. Israeli, and S. A. Orszag. High-order splitting methods for the incompressible Navier-Stokes equations. *J. Comp. Phys.* 97(1):414, 1991.
- ¹⁷Karniadakis, G. E., and S. J. Sherwin. Spectral/hp Element Methods for CFD, 2nd edn. Oxford: Oxford University Press, 2005, 650 pp.
- ¹⁸Kirby, R. M., and G. E. Karniadakis. De-aliasing on non-uniform grids: algorithms and applications. *J. Comp. Phys.* 191:249–264, 2003.
- ¹⁹Köhler, U., I. Marshall, M. B. Robertson, Q. Long, and X. Y. Xu. MRI measurement of wall shear stress vectors in bifurcation models and comparison with CFD predictions. *J. Magn. Reson. Imaging* 14(5):563–573, 2001.
- ²⁰Ku, D. N. Blood flow in arteries. *Annu. Rev. Fluid Mech.* 29:399–434, 1997.
- ²¹Ku, D. N., D. P. Giddens, C. K. Zarins, and S. Glagov. Pulsatile flow and atherosclerosis in the human carotid bifurcation. Positive correlation between plaque location and low oscillating shear stress. *Arteriosclerosis* 5:293–302, 1985.
- ²²Lee, S., S. W. Lee, P. F. Fischer, H. S. Bassiouny, and F. Loth. Intravascular turbulence in a diseased carotid bifurcation: numerical study. World Congress on Medical Physics and Biomedical Engineering, Seoul, Korea. IFMBE Proceedings 14, Springer, Berlin, 2006.
- ²³Lumley, J. L. The structure of inhomogeneous turbulent flow. In: *Atmospheric Turbulence and Radio Wave Propagation*, edited by A. M. Yaglom, and V. I. Tatarski. Moscow: Nauka, 1967, pp. 160–178.
- ²⁴Manhart, M. Vortex shedding from a hemisphere in turbulent boundary layer. *Theoret. Comput. Fluid Dyn.* 12(1): 1–28, 1998.
- ²⁵Private communication with Kutay Ustuner, Scientist, Principal Siemens, Health Care Ultrasound Division.
- ²⁶Sauve, J. S., K. E. Thorpe, D. L. Sackett, W. Taylor, H. J. M. Barnett, R. B. Haynes, and A. J. Fox. Can bruits distinguish high-grade from moderate symptomatic carotid stenosis? *Ann. Intern. Med.* 120(8):633–637, 1994.
- ²⁷Sherwin, S. J., and H. M. Blackburn. Three-dimensional instabilities of steady and pulsatile axisymmetric stenotic flows. *J. Fluid Mech.* 533:297–327, 2005.
- ²⁸Sherwin, S. J., and M. Casarin. Low-energy basis preconditioning for elliptic substructured solvers based on unstructured spectral/hp element discretization. *J. Comp. Phys.* 171(1):394–417, 2001.
- ²⁹Sirovich, L. Turbulence and dynamics of coherent structures: I-III, *Quart. Appl. Math.* 45:561–590, 1987.
- ³⁰Steinman, D. A., T. L. Poepping, M. Tambasco, R. N. Rankin, and D. W. Holdsworth. Flow patterns at the stenosed carotid bifurcation: effect of concentric versus eccentric stenosis. *Ann. Biomed. Eng.* 28(4):415–423, 2000.
- ³¹Stroud, J. S., S. A. Berger, and D. Saloner. Numerical analysis of flow through a severely stenotic carotid artery bifurcation. *J. Biomech. Eng.* 124:9–20, 2002.
- ³²Varghese, S. S., S. H. Frankel, and P. F. Fischer. Direct numerical simulation of stenotic flows. Part 2. Pulsatile flow. *J. Fluid Mech.* 582:281–318, 2007.
- ³³Volino, P., and N. Magnenat-Thalmann. The SPHERIGON: a simple polygon patch for smoothing quickly your polygonal meshes. *Proceedings of the Computer Animation*, 1998, pp. 72–78.
- ³⁴Wang, S., W. Lee, J. Provost, J. Luo, and E. Konofagou. A composite high-frame-rate system for clinical cardiovascular imaging. *IEEE Trans. Ultrason. Ferroelectr. Freq. Control* 55(10):2221–2233, 2008.
- ³⁵www.pointwise.com. Accessed 2 August 2009.
- ³⁶Yakhot, A., T. Anor, and G. E. Karniadakis. A reconstruction method for gappy and noisy arterial flow data. *IEEE Trans. Med. Imaging* 26(12):1681–1697, 2007.